EÖTVÖS LORÁND UNIVERSITY

FACULTY OF INFORMATICS

INSTITUTE OF CARTOGRAPHY AND GEOINFORMATICS

DETECTING GEOLOGICAL FEATURES IN THE AL KUFRAH BASIN USING REMOTELY SENSED DATA

Natsnet Habtit Haile

Student of Cartography MSc

Gáspár Albert, PhD

Associate professor

ELTE Institute of Cartography and Geoinformatics

Budapest, 2022

DECLARATION

I, undersigned NATSNET HABTIT HAILE (NEPTUN CODE: W4ZCNP), declare that the current master's thesis is my original intellectual work and that I have submitted no part or all of it to any other institution. Permissions regarding copyrighted sources for use in this work are attached.

<u>I AGREE</u> to publish the accepted master's thesis in pdf form on the Institute of Cartography and Geoinformatics website.

Budapest, 15th May 2022

(Signature of the student)

ACKNOWLEDGMENT

My heartfelt thanks to everyone who contributed to the success of this thesis project. I wish to thank my supervisor Gáspár Albert for his advice, guidance, and support throughout the thesis work. I want to pass my sincerer thanks to my family for supporting me throughout doing my studies and for their encouragement when I was working on my thesis.

I want to thank all my professors at the ELTE Institute of Cartography and Geoinformatics for instructing me throughout my studies. I also want to thank my friends and course-mates for the assistance they may have given me throughout my studies. Finally, I want to thank the Almighty God for giving me this chance to conduct my studies and research in Hungary.

ABSTRACT

Mineral resources play a significant role in improving the financial situation. Hence for the successful identification, exploitation, and exploitation of the minerals, there is a need to identify the location of these minerals. However, remote sensing techniques such as satellite images are proven reliable methods for exploring these minerals, especially in complex terrain regions.

This study aims to use remote sensing applications in a geological study by developing a technique that can be used to explore the Cenozoic ferruginous sediments in the Al Kufrah Basin, Libya using Sentinel-2 bands. The bands were subjected to various image processing techniques that resulted in choosing false-color composite (FCC) of the band (12-8-3) to enhance lithology, band ratio images of (4/2-11/8-11/12) for iron deposits, Principal Components Analysis (PCA) and unsupervised classification (K-mean and Iso-data) helped identify different lithologies. Lithologic maps and the ferruginous sediments identified by image processing techniques agree with geological maps.

The iron concentrated ferruginous sediments are widely spread from less to high concentrations toward the NE of the study area. Given the spread of the sediments, the iron deposit may extend beyond the sand-covered area. The study can improve a new potential map of iron ore deposits in a new location.

Keywords: Sentinel-2, Ferruginous sediments, Iron, Image Analysis, Libya

Table of Contents

List of Figures and Tables

List of Figures

List of Tables

Abbreviation and Acronyms

ANN	-	Artificial Neural Network
ASTER	-	Advanced Space-borne Thermal Emission and Reflection radiometer
BOA	-	Bottom of Atmospheric
BR	-	Band Ratio
CIVB	-	Central Iranian Volcanic Belt
DPA	-	Direct principal analysis
EM	-	Expectation Maximization
ENVI	-	Environment for Visualizing Images
ENVI	-	Environment for Visualizing Images
ERS	-	European Remote Sensing satellite
ETM+	-	Enhanced Thematic Mapper plus
FCC	-	False color composite
FIR	-	Finite Impulse Response
GIM	-	Gossan Index minerals
GIM	-	Gossan Index Minerals
GIS	-	Geographic Information System
ICA	-	Independent Component Analysis
ISODATA	-	Iterative Self-Organizing Data Analysis Technique
K-NN	-	K- Nearest Neighbors
LCS	-	Land Cover Signature Classification
MLC	-	Maximum Likelihood Classifier
MSI	-	Multi-Spectral Instrument
OBIA	-	Object-Based Image Analysis
OLI	-	Operational Land Ima
PC	-	Principal Component
PCA	-	Principal Component Analysis
QGIS	-	Quantum GIS

RFC	-	Random Forest Classifier
RGB	-	Red, Green, and Blue
RS	-	Remote Sensing
SPOT	-	Satellite Pour l’Observation de la Terre
SVM	-	Support Vector Machine
SWIR	-	Short Wave Infrared
TIR	-	Thermal infrared
TM	-	Landsat Thematic Mapper
UTM	-	Universal Transverse Mercator
VNIR	-	Visible and near-infrared
WGS	-	World Geodetic System

CHAPTER ONE: INTRODUCTION

1.1 Research Background

Deserts exist on every continent and cover more than 30% of the Earth's land surface. The Sahara Desert is one of the biggest deserts in the world, which has undergone major hydrological fluctuations and was vegetated in the past. When the wet time frames finished at about 5.5 ka, the Sahara had changed into a hyper-arid desert, and its unique surface and alluvium-filled valleys and lake basins were covered with windblown sand sheets and dune fields (E. Ghoneim et al., 2012). Although they typically do not have many inhabitants, they are often the loci of economic and cultural activity.

Notably, mineral resources play a significant part in the practical financial improvement of nations. Nonetheless, the distribution of a mineral resource varies in geological settings and requires exceptionally efficient discovery techniques. Identifying the indicators of geological structures is important in exploring and exploiting resources in Libya. The size, remoteness, and harsh nature of many of the country's deserts make it difficult and costly to map or monitor these landscapes on the ground. Innovation in spatial techniques is required for mapping geological features which face many social and environmental constraints (Ibrahim et al., 2018).

Mohamed et al. (2021) agree that remote sensing is more cost-effective, and data can be collected on a large scale at regular intervals, which opened an era of lithological mapping by means of remote sensing. The significant expense associated with the investigation of mineral resources by conventional methods influences the economic returns of mining. Remote sensing is a significant tool for the initial recognition of structures, especially in regions that are comprised of a similar rock as the surroundings, which adds to the decrease of cost and time during prospecting fieldwork (Ghoneim, 2018; Koeberl et al., 2005).

Geologists have conducted mineral mapping and lithological unit discrimination using satellite acquired data that show successful discrimination results from Advanced Spaceborne Thermal Emission and Reflection Radiometer (ASTER) sensors over Landsat Thematic Mapper (TM), Enhanced Thematic Mapper Plus (ETM+), Operational Land Imager (OLI) (Tangestani et al., 2008). However, there is a need to investigate the performance and efficiency of recent satellites such as Sentinel-2 in compiling geologic and lithologic maps (Tangestani & Shayeganpour, 2020).

This will bring in new knowledge on the variance of results and provide the basis for comparing the accuracy of identifying geological deposits on the Earth's surface.

Several remote sensing techniques have been carried out for geological and structural mapping in the Sahara region. Also, remote sensing studies have been done around Al Kufrah Basin (e.g. E. M. Ghoneim, 2009; Schmieder et al., 2009; Albert et al., 2016, Alasta, 2011, Abulghasem et al., 2012). These investigations have been done based on Landsat ETM+, dual-band (L and C) and dual-polarization (HH and HV) radar (SIR-C), and SRTM data. Lithological classification using Sentinel-2, ASTER, and OLI data has been carried out also in other parts of the world, such as the Gobi Desert in China and the Central Iranian Volcanic Belt (CIVB) (Ge, W et al., 2018; Khaleghi et al., 2020)

A study to examine prospects of carbonate-hosted Pb-Zn minerals was done in the central Iranian terrain using Sentinel-2 (bands 2, 3, 4, 11, and 12), ASTER (VIR+SWIR bands), and Landsat-8 (OLI bands) images while utilizing Principal Component Analysis (PCA) (Sekandari et al., 2020). Principal components represent relevant substances' spectral responses and mineral spectral information (El Atillah et al., 2019). Hydrothermal alteration zones were mapped using infrared bands of (0.45-1.0 µm) for OLI and Sentinel-2 images, while ARSET used a wavelength of 1.65 and 2.43 µm (Khaleghi et al., 2020). The study further states that mapping results for iron oxide minerals were better for Sentinel-2 images than ARSET and OLI data. Moreover, Mielke et al. (2014) found that Sentinel-2 sensors were better equipped for iron depth measures than current multispectral sensors.

Image classification techniques are divided into three types: unsupervised image classification, supervised image classification, and object-based classification (GISGeography, 2021). Unsupervised classification uses algorithms such as K-means and ISODATA to generate Iso clusters and classify the clusters. Supervised classification uses training sites or samples to classify the image. Object-Based Image Analysis (OBIA) uses segmentation algorithms and groups pixels to create objects with a vector shape.

El Atillah et al., 2019 concluded that Sentinel 2A, Landsat 7 and 8, and ASTER images provide good mapping results for lithology and mineralogical alteration while using unsupervised classification. This study utilized K-means, Isodata, thresholding, watershed, efficient graph-based image segmentation, and algorithms for geological mapping. However, it was concluded that the K-means and Isodata algorithms were the best for lithological discrimination.

Prediction of iron oxides and clay minerals was made using Sentinel 2 images while computing band ratios, RGB combinations, principal component analysis (PCA), and image classification (Cardoso-Fernandes, J., Teodoro, A., & Lima, 2018). In the RGB combination, the clay and carbonates have a reflectance of 1.55 to 1.75 μm and absorption of 2.1 to 2.4 μm, while iron oxides and sulphate minerals have a high reflectance in near-infrared and low blue reflectance. The study used a band ratio of 4/2 to map iron oxides because of absorption features in band 2 (blue) and high reflectance in band 4 (red). Image analysis was applied on PCA for all six bands.

Bas Draa inlier lithological units mapping was done using ASTER and OLI data, and the image classification utilized PCA, band ratio (BR), and Support Verctor Machine (SVM) (Adiri et al., 2016). PCA and BR results showed excellent correlation with available geological of the area with a high Kappa coefficient accuracy. This study concluded that BRs and PCA gave good results than SVM classification.

1.2 The Study Area

The materials processed in the present study were collected during a scientific project started in 2008 by Industrial Research Center, Libya, and ErPetro Ltd. Hungary under the contract of "Scientific and technical cooperation in geological mapping Al Kufrah Basin." The project aimed to compile twelve geological maps at a scale of 1:250,000 covering the Kufrah Basin (Albert et al., 2016). The details of the map sheet are explained in table 3. The expedition revealed proof of a Tertiary geological formation containing sedimentary Iron (laterite).

By using multispectral satellite image classification, iron-containing surface materials can be revealed (Van der Meer et al., 2014; Albert & Ammar, 2020). Multispectral datasets, like Landsat Thematic Mapper (TM) and Landsat Enhanced Thematic Mapper Plus (ETM+) have been used to discriminate and interpret various lithology and structures (Loughlin, 1991; Liu et al., 2007) for several years; other multispectral sensors such us Advanced Space bone Thermal Emission and Reflection (ASTER) were also used for surface mapping.

The presence of excellent exposure with less vegetation cover makes the use of remote sensing technique for the identification of geological features in Libya, to be specific in the study area (Al

Kufrah Basin). This study aims to use remote sensing data in a geological study by applying a technique that can be used in the exploration of ferruginous sediments. Moreover, the study aims to identify minerals and will help to assess the use of multispectral datasets and spectral signatures.

1.3 General Objectives

The thesis aims to analyze satellite images of the study area to identify the known - and supposed - occurrence of the Early and Late Cenozoic continental sediments. The work includes building a geodatabase of the mapped (known) occurrences based on the maps of the joint Libyan-Hungarian expedition, the analysis of satellite images, and the unsupervised classification of the images. The main objectives are listed below.

- Identify and mapping of the ferruginous concentrated iron sediments associated with the deposit in the Al Kufrah Basin.
- Characterize spectral reflectance of the different geologic features, validate the map with the satellite image result and execute the unsupervised classification on remotely sensed data.
- Evaluate the effectiveness and accuracy of unsupervised classification techniques in geologic investigations.

1.4 Thesis organization

This thesis is prepared as a chain of connected chapters. After a short introduction in Chapter one, the geologic setting and remote sensing with prior information in the area are defined in Chapter two. Collected data and several image processing techniques applied are detailed in Chapter three. The result of the ferruginous sediments and lithology are discussed in Chapter four. The conclusions drawn collectively with suggestions are eventually presented in Chapter five.

CHAPTER TWO: GEOLOGIC SETTING AND REMOTE SENSING

2.1. Geologic Setting

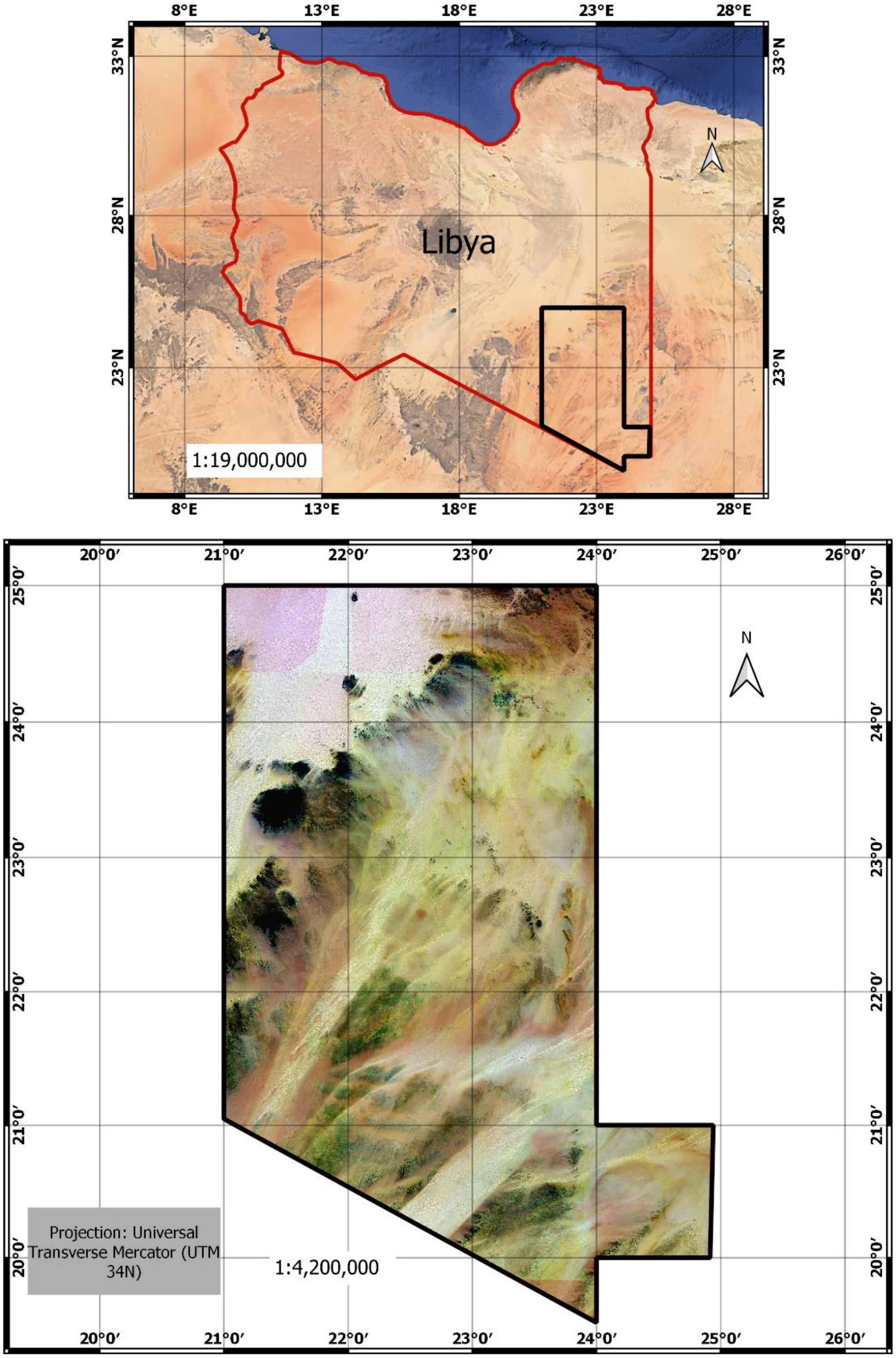

Figure 1. Location map of the study area in RGB (12-8-3) of Sentinel-2 bands

The study area lies between latitudes 19º00’ and 25º00’ 20º00’ N, longitudes 21º00’ and 25º00’ E, and is roughly 173 000 square km in size characterized by vast, low relief that gently dipped to the North. Figure 1 shows the area of interest is the Al Kufrah Basin, Libya, which covers various lithologies, including Quarat al Hamra Formation, Al Jawf Formation, Eolian sediments, Playa sediment, Serir and Gravity driven deposits (Table 7). More than a decade ago, a joint Libyan-Hungarian expedition identified characteristic Cenozoic sediments within the area, which were previously unknown and named Idris formation (CzI), and undivided Cenozoic continental sediments (Czc). The majority of the Al Kufrah Basin was occupied by continental environments during the Paleogene and Neogene periods. Instead of forming in rivers, as they did in the Mesozoic, the sedimentary units of this period originated in paludal environments, and they were only preserved in small-scale subsiding basins that subsequently reversed geographically. The Cenozoic sediments are primary and secondary (redeposited) remnants of tropical soils developed on the Mesozoic sandstone surfaces in the early Tertiary. Those ferruginous sediments accumulation was observed NE and SE of the study area surrounded by early deposits of sand and silt sediments. The laterite and the high iron content are the most characteristic in these sediments, and these are also the most detectable lithological features on the multispectral images. The Idris formation is characterized by locally redeposited, in situ weathering product, laterite, duricrust, ferruginous sediments, and the Cenozoic continental sediments are characterized by locally cemented, gravel, rock debris, sand, silt, ferruginous sediment. The Al Kufrah Basin, in general, covers various lithology (after Albert et al., 2016).

2.2. Remote sensing in geological exploration

RS techniques have typically played an essential part in geologic exploration because they’re practical methods of measuring many relevant physical properties of large, inaccessible areas (Colwell, 1983). Remote sensing is the handiest far-flung exploration technique that maps the broad range of alteration minerals related to many ore deposits (Agar & Coulter, 2007). Geological mapping is evolving from the conventional field survey to the use of remote sensing technologies (Abdunaser, 2015). Remote sensing from space offers a unique opportunity to study the desert environment on a regional basis because climatic conditions are nearly always favorable to monitoring from space (Y. E. Abdelhady, 1978). Satellite and airborne multispectral or hyperspectral sensors were substantially used to assess numerous lands, sea, and atmospheric features (Memarsadeghi et al., 2003; Ciampalini et al., 2013).

Remote sensing records are used for mineral exploration to map geology and structures using their spectral signature. The visible and near-infrared wavelengths and the shortwave infrared region are frequently utilized in geological applications. The band used is decided based on the spectral signature of the rocks.

The reflection spectra of rock are determined by its mineralogical composition. Mineral absorption of electromagnetic waves in the visible and short-wavelength infrared is affected by chemo-electronic and vibrational processes induced by the molecular structure. Weathering of minerals produces ferrous iron (Fe2+), which makes absorption troughs at 0.45, 1.0–1.1, 1.8–1.9, and 2.2–2.3 micrometer. The ferric iron (Fe3+) has absorption troughs at about 0.65 and 0.87 micrometers, as shown in figure 2 (Abrams et al., 1988; Rajendran et al., 2011).

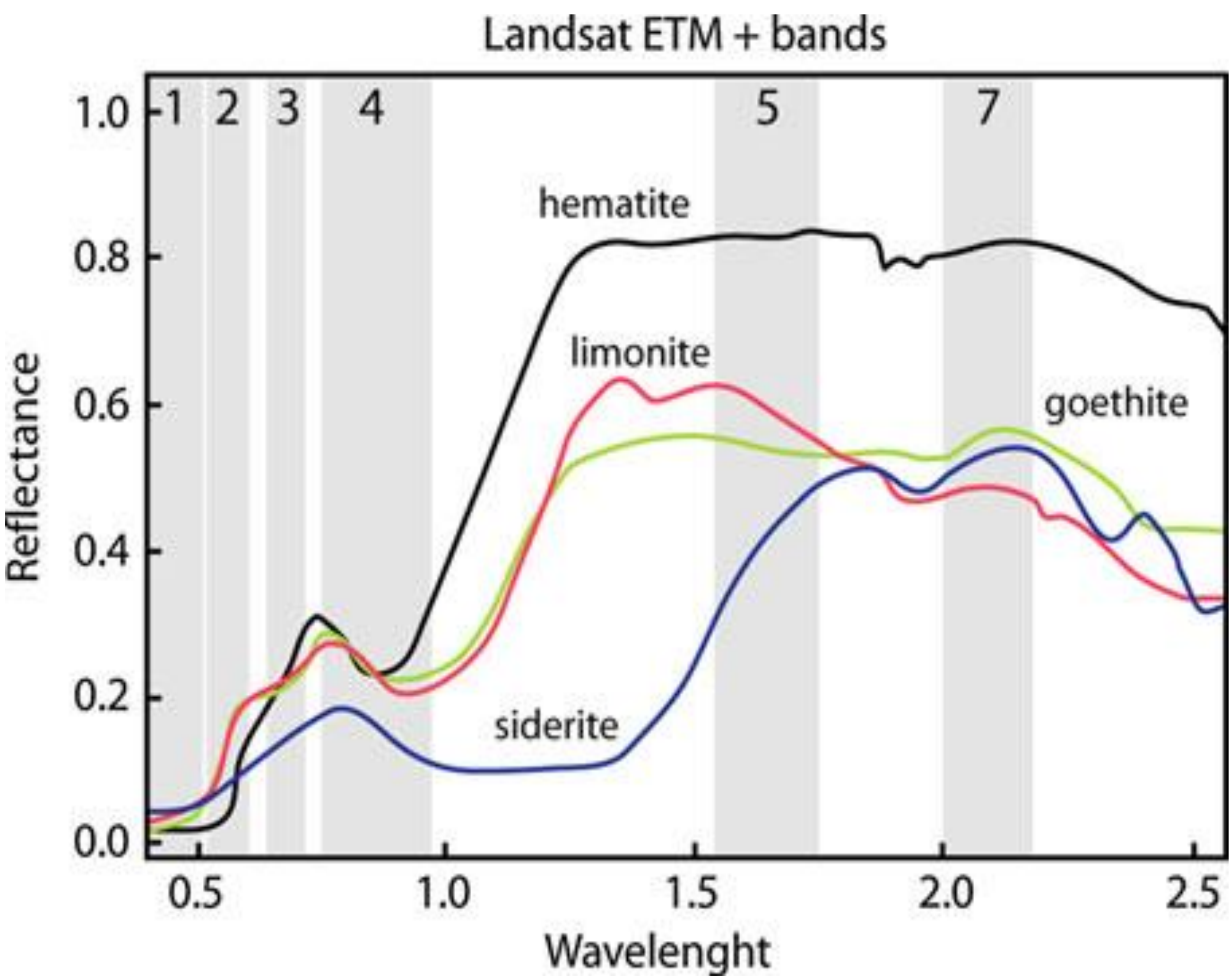

Figure 2. Offset spectral plots of major iron minerals from the USGS mineral spectral

Geological features can be detected using remote sensing data such as satellite and radar images, especially where the vegetation cover is sparse (Van der Werff & van der Meer, 2016; Albert & Ammar, 2020). The multispectral images can be used in the classification of the surface, and based on the applied band calculations, different features can be outlined, enhanced, or subverted. The detectable geological features are usually expressed as abrupt and characteristic lithological changes and may identify most often as sedimentary layer boundaries, prominent beds, intrusions, or tectonic lines.

Image classification techniques for geological mapping depend on the type of mineral being investigated. A comparison of multispectral data imagery classification accuracy showed that the Sentinel-2 result was 74.5%, which was 5.8% and 2.5% higher than OLI and ASTER images, respectively (Ge, W et al., 2018). Mielke et al. (2014) concluded that the mean accuracy for iron absorption mapping of mine waste minerals was Sentinel-2 94.5%, OLI 92%, ASTER 88.5%, and ETM+ 83%. This is evidence that the Sentinel sensor has a high accuracy compared to the other sensors listed. Cardoso-Fernandes et al. (2018) concluded that Sentinel-2 data is a good source of data for mineral exploration.

Sentinel 2-A data is theoretically suggested to be more advantageous in lithological classification than Landsat and ASTER images due to its higher spatial and spectral resolutions (Tangestani & Shayeganpour, 2020). The fine spectral resolution of Sentinel-2 images in the SWIR region (75–242 nm) and in the visible and near-infrared (VNIR) region (18–145 nm) makes it suitable for geological analysis and mapping. Sentinel-2 also has a super-spectral design which provides VNIR narrow bands that allow for iron absorption at 0.9 µm wavelength (van der Werff & van der Meer, 2015).

Furthermore, the satellite images fully cover the Earth with a spectral resolution of 13 bands and spatial resolution of 10m, 20m, and 60m with a swath width of 290 km, which is larger than Landsat and SPOT (European Space Agency, 2022). They are also freely available online, making conducting research with them conducive. A summary of the bands, swath width, and spatial resolution of Landsat 8 (OLI), ASTER, and Sentinel-2 are given in table 1 below (Van der Meer et al., 2014; van der Werff & van der Meer, 2016; Khaleghi et al., 2020).

Table 1. Characteristics of ASTER, Landsat 8, and Sentinel-2 data

Characteristic		Landsat 8 (OLI)	ASTER	Sentinel-2A
Bands		11	14	13
Swath width (km)		185	60	290
Spatial resolution	VNIR	30m	15m	10m, 20m, 60m*
	SWIR	30	30	20
	TIR	100	90	-
	PAN	15	-	-
***10m (B2, B3, B4, B8); 20m (B5, B6, B7, B8a); 60m (B1 and B9)**				

Iron ore makes up about 8% of the Earth's crust; hence it's relatively abundant on the Earth's surface. Specific wavelengths have been suggested for proper mapping of iron ore using satellite images on the Earth's surface. Vincent (1997) noted that ferric (Fe^{3+}) and ferrous (Fe^{2+}) iron ions in iron oxides and mafic silicates, hydroxyl (OH-1) ion in hydroxides and clays, H_2O in hydrated minerals, the carbonate CO3-2 ion in carbonate minerals, and the sulfate SO4-2 ion in sulfate minerals absorb light at a different wavelength. Depending on the lattice environment Ferrous iron (Fe^{2+}) produces absorption centered around 0.45 µm, 1.0–1.1 µm, 1.8–1.9 µm, and 2.2–2.3 µm wavelength, while Ferric iron (Fe^{3+}) produces absorptions of wavelength between 0.65 µm, and 0.87 µm (El Zalaky M.A et al., 2018).

Different image analysis techniques have been used for feature extractions in remote sensing. PCA is widely used in feature extraction methods. This technique builds new spatial representations for spectral bands using an inter-band covariance matrix (Marrakchi et al., 2021). And different types of image classification methods have been used in various geologic studies; Ge, W et al. (2018) supervised the classification of 15 lithological units using machine learning methods such as Artificial Neural Network (ANN), K- Nearest Neighbors (K-NN), Maximum Likelihood Classifier (MLC), Support Vector Machine (SVM), and Random Forest Classifier (RFC) which are supervised classification methods. MLC and SVM methods showed similar and better results than K-NN, ANN, and RFC techniques for geological mapping. Nivedita Priyadarshini et al. (2018) further support this by stating that the MLC has a high accuracy of 89.30% for supervised classification. Supervised classification using Land Cover Signature Classification (LCS) and the Maximum Likelihood was performed on six PCs to map iron oxide and clay minerals (Cardoso-Fernandes et al., 2018). El Atillah et al. (2021) note that there is great capacity for geological discrimination and segmentation using unsupervised classification techniques such as K-Means and Isodata algorithms, which yield similar image classification results. On the other hand, Aydda et al. (2020) concluded that the Iso Data unsupervised classifier showed high performance when detecting barchan dunes over K-Means, Expectation-Maximization (EM).

2.3. Image Analysis Techniques

2.3.1. Band Ratio (BR)

Band ratio is an image enhancement technique that results by dividing one spectral band by another; it produces an image that provides relative band intensities. Band ratios play a crucial role in separating mineral varieties and vegetation density by amplifying the coefficient of reflection divergences between the required bands while subduing the effects of topography and brightness (Abrams et al., 1983). This raised discrimination is a result of the fact that ratio images distinctly constrain the variations in the slopes of the two spectral reflectance curves bands involved, irrespective of the absolute reflectance values discovered in the bands (Lillesand et al., 2004).

Table 2. Sentinel-2A MSI and Landsat-8 OLI band ratios, as an analogue of Kalinowski and Oliver's (2004) ASTER band ratios used as proxies for mapping mineralogy (After Van der Meer et al., 2014, later modified by van der Werff & van der Meer, 2016)

Feature	ASTER	Landsat 5 TM	Landsat 8 OLI	Sentinel-2A MSI
TM Ratios				
Hydroxyl bearing alteration	4/{5,6,7}	**5/7**	6/7	11/12
All iron oxides	–	**3/1**	4/2	4/2
Ferrous iron oxides	2/4	**3/5**	4/6	4/11
ASTER Iron				
Ferric Iron, Fe^{3+}	**2/1**	3/2	4/3	4/3
Ferrous Iron, Fe^{2+}	**5/3 + 1/2**	7/4 + 2/3	7/5 + 3/4	12/8 + 3/4
Laterite	**4/5**	5/7	6/7	11/12 †
Gossan	**4/2**	5/3	6/4	11/4
Ferrous silicates ‡	**5/4**	7/5	7/6	12/11 †
Ferric oxides	**4/3**	5/4	6/5	11/8
ASTER Silicates				
Alteration	**4/5**	5/7	6/7	11/12 †
ASTER Other				
Vegetation	**3/2**	4/3	5/4	8/4
NDVI *	**(3 − 2)/(3 + 2)**	(4 − 3)/(4 + 3)	(5 − 4)/(5 + 4)	(8 − 4)/(8 + 4)

† Band 12 of Sentinel-2A MSI and band 7 of Landsat 8 OLI cover ASTER bands 5–7. Landsat 5 TM band 7 also partially covers ASTER band 8; ‡ Biotite, chloride and amphibole; * Normalized Difference Vegetation Index.

Multispectral remote sensing research requires analysis of band ratios, especially in geological mapping of different minerals (Yamaguchi, 2001). According to the band ratio, in one band, the mineral has higher reflectance characteristics, while in another band, the same mineral has high absorption characteristics (Kalinowski & Oliver, 2004). Several band ratios are proposed for Sentinel-2 to derive the following products: ferric iron, ferrous iron, laterite, gossan, ferrous silicate, and ferric oxides (Van der Meer et al., 2014). The modified band ratio for mineralogical mapping is seen in table 6.

2.3.2. False Color Composite (FCC)

False-color composite (FCC) images are representations of multispectral images produced with bands aside from visible red, green, and blue as the display's red, green, and blue components. False-color composites allow us to see wavelengths that are invisible to the naked eye (i.e., near-infrared and beyond). Using bands such as near-infrared emphasizes spectral variations and improves the data's interpretability. False-colored composites come in a variety of colors and can be used to spotlight various features.

For displaying a false-color composite (FCC), we need to select three spectral bands or ratio images based on the known reflectance or absorption feature of a mineral. As penetration intensity is a function of geologic materials and different polarization modes, the combination of different bands as Red, Green, and Blue (RGB) provides direct but qualitative information about different geological materials in the subsurface (Van Gasselt et al., 2017). A false-color composite image of bands 7, 4 & 1 in the RGB using linear contrast enhancement was used for ETM+ bands (A. Ali, 2012); he as well created a false-color band ratio combination of 5/7, 3/1, 3/5 (after Sabin's ratio) as RGB. E. Ghoneim, 2018 uses an RGB color composite image of Sentinel -1 to reveal the morphology of a large part of the Rimaal (Sand) structure concealed beneath the Sahara Aeolian sand eastern part of Sahara. The eight bands were subjected to various statistical analyses, which resulted in the selection of Multispectral Landsat ETM+ data bands (7, 4, and 2) assigned to red, green, and blue, respectively, for iron deposits in Wadi Shati, Libya (Abulghasem et al., 2012). Fuzzy logic modeling was used to create RGB false-color-composite from bands 2, 8, and 12 for Sentinel-2, bands 2, 5, and 7 for Landsat-8, and bands 6, 2, and 8 for ASTER images for showing the lithological units having spectral features related to Fe3+ and Fe3+/Fe2+ iron oxides and clay and carbonate minerals (Sekandari et al., 2020).

2.3.3. Principal Component Analysis (PCA)

Principal Components Analysis (PCA) is an ordination approach that takes a variable dataset and reorients it in such a way that the axis of greatest variance becomes the first principal component (PC), and the axis of second-greatest variance becomes the second PC, and so on (Gazley et al., 2015). PCA is used to enhance and separate spectral signatures from the background and identify qualitative differences in lithology (Salehi et al., 2019). This is done by identifying large amounts of variation in the data and creating new uncorrelated components. Richards & Xiuping (1999) found that the first principal component (PC) band has the most variance, the second PC band has the second-highest variance, and the last PC band has the lowest variance and the highest noise (Oppenheimer, 2000). PCA selects principal components (PC), which are uncorrected linear variables, and uses orthogonal transformations (Richards, 2013).

The use of the PCA technique for alteration mapping has gotten a lot of attention. To extract mineral information from multispectral data, PCA can be used (Crósta, A. P., Moore, 1989; (Loughlin, 1991). Chen et al., 2017 used the PCA approach to extract ferrous and hydroxyl modifications from Sentinel-2 data. And for Gossan Index Minerals (GIM), such as hematite, jarosite, and goethite mapping, the principal component analysis (PCA) method was used to enhance interest targets by reducing spectral tendencies and noise components, thereby creating images and new PCs based on band ratio and combination (Masoumi et al., 2016; Khaleghi et al., 2020). Salehi et al. (2019) further indicated that lithological units are best discriminated using bands with large data variance. This method has yielded effective results in mineral exploration and geological discrimination results ((El Atillah et al., 2019). PCA has also been utilized with multispectral data by several academics (Mia, B., Fujimitsu, 2012; Gabr, S., Ghulam, A., 2010; Ghulam, A., Amer, R., and Kuksy., 2010; Amera, 2007)

2.4. Image Classification

Image classification is a technique that assigns land cover classes to pixels based on their attribute values. A pixel is allotted to the class to which its attributes, such as multispectral response, are most similar. It can also be defined as a data reduction method that converts remote sensing images into thematic data. The three main techniques for image classification in remote sensing are Unsupervised, Supervised, and Object-based image analysis. The two most typically used image classification is Unsupervised and Supervised image classification. In this project, unsupervised image classification has been done.

2.4.1. Unsupervised Classification

Unsupervised classification is a key tool in image processing for geoscience and remote sensing applications, and it's employed when reliable data is few or unavailable (Memarsadeghi et al., 2003). Unsupervised classification first divides pixels into "clusters" depending on their properties, then assigns a land cover class to each cluster. The following are the stages required for unsupervised classification:

- **Generate clusters**: In this step, the program clusters pixels into a set number of classes. So, step one is to assign the range of classes you want to generate. Also, you must identify which bands you need to use. The steps are:
  - Input: this is to input the image needed to be classified
  - Number of classes: Choose some number of classes needed to generate during the unsupervised classification
  - Minimum class size: It's the number of pixels to make a unique class
- **Assign classes**: this is the level at which you have to identify each class from the output iso-clusters. The steps are:
  - Select color for each class
  - After setting the colors for each class, it can be merged with each of your classes, and we can merge the classes using the reclassify tool.

The use of unsupervised classification is to investigate and cluster unlabeled datasets. The applied methods discover hidden patterns or data groupings without the requirement for human intervention. El Atillah et al. (2019) used Iso-data and K-Means classification on Sentinel-2 for mapping the hydrothermal alteration zone mapping. The two types of classification are discussed below:

2.4.1.1. K-Means

K-mean is one of the unsupervised classification procedures. This method's classification principle is to classify pixel values based on K values, which are the desired number of classes or clusters (Nurdin et al., 2019). It's a clusterization method that groups object by minimizing the sum of quadratic or Euclidean distance between each object and the cluster centroid or group. K-Means cluster homogeneous pixels based on the center pixel (Nivedita Priyadarshini et al., 2018). With clustering, we can quickly partition data into clusters equal to or more than the number of classes, making it ideal for classification.

2.4.1.2. Iso-data

Iterative Self-Organizing Data Analysis Technique (ISODATA) classification is one of the unsupervised classification methods in which the principle is to classify pixel values based on a mean value into certain groups/clusters. The Iso-data algorithm works by grouping similar clusters and data in clusters so that they can be divided according to the maximum standard deviations (Wang, 2016). This algorithm is based on optimal thresholding by using a criterion function to measure the statistical separation between two regions (El Atillah et al., 2021). The first principal components usually apply the Iso-data technique to reduce processing load.

Table 3. Geological map sheet of Kufrah basin by the industrial research center of Libya

GEOLOGICAL MAP SHEETS COVERING THE KUFRAH BASIN ON A SCALE OF 1:250,000 (2016)		
NO.	Map Sheet	Author
1	Bir as Sulaya (NF 34-7)	Loránt M., Mabrouk JB. (eds.), Albert G., Csillag G., Csontos P., Elgrewi AM., Fodor L., Kalmár J., Lantos Z., Trish KB., El-Mehdi BO. 199P
2	Jabal ash Sharif (NF 34-8)	Lantos Z., Réti Zs., Trish KB. (eds.), Fodor LI., Albert G., Csillag G., Loránt M., Kalmár J., Csontos P., Koloszár L., Mabrouk JB., Elgrewi AM.178P
3	South al Kufrah (NF 34-4)	Kalmár J., Loránt M. Elgrewi AM (eds.), Lantos Z., Albert G., Fodor LI., Réti Zs., Csillag G., Csontos P., Mabrouk JB., Trish KB., El-Mehdi BO. 199P
4	Hassi Nafou (NF 34-3)	Albert G., Mabrouk JB. (eds.), Császár G., Fodor L., Kalmár J., Loránt M., Csontos P., Trish KB. Elgrewi AM., El-Mehdi B. 140P
5	Matan as Sarah (NF 34-11)	Lantos Z., El-Grewi AM. (eds.). Albert G., Császár G., Csillag G., Csontos P., El-Mehdi B., Fodor L., Kalmár J., Koloszár L., Loránt M., Mabrouk JB., Réti Zs., Trish KB. 217P
6	Rabyanah (NG 34-15)	Albert G., El-Mehdi BO. (eds.), Fodor L., Kalmár J., Loránt M., Csontos P., Trish KB., El-Grewi AM. 137P
7	Al Kufrah (NG 34-16)	Császár G., El-Mehdi BO. (eds.), Kalmár J., Fodor L., Albert G., Lantos Z., Csillag G., Csontos P., Loránt M., Trish KB., Mabrouk JB., El-Grewi AM. 243P
8	Matan Al Sarah (NF 34-12)	Lantos Z., Mabrouk JB. (eds.). Albert G., Csillag G., Csontos P., El-Grewi AM., El-Mehdi BO., Fodor L., Kalmár J., Koloszár L., Loránt M., Réti Zs., Trish KB. 255P
9	East Irq Al Idrisi (NF 35-13)	Albert G., Trish KB. (eds.), Császár G., Csillag G., Csontos P., El-Grewi AM., El-Mehdi BO., Fodor L., Kalmár J., Loránt M., Mabrouk JB.133P
10	West Irq al Idrisi (NF 34-15)	Réti Zs., Mabrouk JB. (eds.), Koloszár L., Kalmár J., Fodor L., Lantos Z., Albert G., Csillag G., Csontos P., Trish KB., El-Grewi AM., Lóránt M., El-Mehdi BO.175P
11	Irq al Idrisi NF (34-16)	Réti Zs., Trish KB. (eds.), Lantos Z., Kalmár J., Fodor L., Csillag G., Albert G., Csontos P., Mabrouk JB., El-Mehdi BO.191P
12	South Irq al Idrisi (NE 34-4)	Réti Zs., Trish KB. (eds.), Lantos Z., Koloszár L., Kalmár J., Albert G., Csillag G., Csontos P., Loránt M., Mabrouk JB., El-Grewi AM., El-Mehdi BO. 178P

CHAPTER THREE: MATERIALS AND METHODS

3.1. Sentinel-2 image data

The datasets used within the thesis encompass Sentinel-2A images and a 12 geological map series of Libya 1:250,000 by Industrial Research Center, Libya, and Er-Petro Ltd. in 2008 (Table 3). Sentinel-2A images are high-resolution multispectral imagery that is undertaken by the Copernicus Program Https://scihub.copernicus.eu/dhus/#/home. The mentioned website already corrects the satellite images. Sentinel-2 delivers reflectance data cubes that exclude atmospheric influences such as water vapor or aerosol correction, allowing end customers to receive ready-to-use products (Soydan et al., 2021). The acquisition date was from 13th November 2020 to 24th February 2020. The subset of thirty-two (32) satellite images was acquired to cover the study area (Table 4). The Sentinel image used is a level -2A with the bottom of atmospheric (BOA) reflectance. The images vary in their spectral resolution depending on the band can be seen in table 5.

As a new mission, the Sentinel satellites can provide regular ordinary observations and data continuity from the previous mission of the European Remote Sensing satellite (ERS), SPOT, ASTER, etc. (Van der Meer et al., 2014). The Sentinel 2A was launched on 23 June 2015, carrying a single Multi-Spectral Instrument (MSI); it comprises 13 spectral bands VNIR bands (B2, B3, B4, and B8) at 10m resolution, red edge bands (B5, B6, B7, B8a) at 20m resolution, SWIR bands (B11 and B12) at 20m resolution, aerosol band (B1) at 60m resolution, water vapor band (B9) at 60m resolution and cirrus SWIR (B10) at 60m resolution. Sentinel-2 band combinations give specific information such as natural color (B4, B3, B3), color infrared (B8, B4, B3), short-wave infrared (B12, B8A, B4), agriculture (B11, B8, B2), geology (B12, B11, B2), Bathymetric (B4, B3, B1), vegetation Index (B8-B4)/(B8+B4), and moisture Index (B8A-B11)/(B8+B11) (GISGeography, 2021). Sentinel-2A and Sentinel-2B, launched on 7 March 2017, comprise a system of twin-polar orbiting satellites, phased at 180^{o} to each other, and the cooperation of twin satellites provides a temporal resolution of 5 days (Lin et al., 2019).

The Sentinel-2A bands were mosaiced and clipped at Environment for Visualizing Images (ENVI) 5.3 to cover the desired area. And QGIS 3.16 was used for resampling and stacking on the desired resolution. This resampled data gives detailed information as it contains a smaller grid size.

Table 4. Data set and source of Sentinel-2A images for the study area

Satellite	Sensor ID	Layers	Date of acquisition	Grid cell size	Product level
Sentinel -2A	T34QEH_20210112T090331 T34QEJ_20210112T090331 T34QEK_20210102T090351 T34QEK_20210105T091351 T34QEL_20210102T090351 T34QEL_20210214T091051 T34QEM_20201213T090351 T34QEM_20210214T091051 T34QFG_20210112T090331 T34QFH_20210112T090331 T34QFJ_20210313T085741 T34QFK_20210201T090211 T34QFL_20210201T090211 T34QFM_20210201T090211 T34QGG_20201230T085351 T34QGG_20210112T090331 T34QGH_20210122T090301 T34QGH_20210129T085221 T34QGJ_20201203T090341 T34QGJ_20210218T085021 T34QGK_20201230T085351 T34QGK_20210102T090351 T34QGL_20210102T090351 T34QGM_20210201T090211 T34QHG_20210208T085121 T34QHH_20201130T085331 T34QHJ_20210208T085121 T34QHK_20210129T085221 T34REN_20210105T091351 T34REN_20210122T090301 T34RFN_20201213T090351 T34RGN_20201213T090351	13	13/11/2020 - 24/02/2021	10 (m)	Level 2A

(Source: Https://scihub.copernicus.eu/dhus/#/home)

The bands used for the study areas include both VNIR bands (B2, B3, B4, and B8) at 10m resolution, and red edge bands (B5, B6, B7, B8a) at 20m resolution, SWIR bands (B11 and B12) at 20m resolution. The Sentinel-2A images have been resampled with the nearest neighbor method to a high resolution of 10 m instead of 20/30/60 m to provide information on the lithology for prospecting and exploration purposes. The data was projected to Universal Transverse Mercator (UTM) projection (WGS 84, zone 34N).

Table 5. Wavelength and bandwidth of the spatial resolution of the MSI instrument

Spatial Resolution (m)	Band Number	S2A		S2B	
		Central Wavelength (nm)	Bandwidth (nm)	Central Wavelength (nm)	Bandwidth (nm)
10	2	492.4	66	492.1	66
	3	559.8	36	559.0	36
	4	664.6	31	664.9	31
	8	832.8	106	832.9	106
20	5	704.1	15	703.8	16
	6	740.5	15	739.1	15
	7	782.8	20	779.7	20
	8a	864.7	21	864.0	22
	11	1613.7	91	1610.4	94
	12	2202.4	175	2185.7	185
60	1	442.7	21	442.2	21
	9	945.1	20	943.2	21
	10	1373.5	31	1376.9	30

(Source:https://sentinel.esa.int/web/sentinel/missions/sentinel-2/instrument-payload/resolution-and-swath)

Generally, multispectral satellite image allows for the detection of hydrothermal alterations and lithological units and non-geological features based on the spectral signature of their wavelength. And Sentinel-2 images are used as they are capable or best used for mineral exploration and hydrothermal alteration zones as they have wide electromagnetic regions with specific information. A geological map of the study area has been used for reference and validation.

3.2. Software

The software used for the research and flow chart of the workflow is mentioned below: (I) ENVI (Environment for Visualizing Images) version 5.3.0 for clipping, mosaicking, image processing, and analysis of multispectral images; (III) Quantum GIS (QGIS) version 3.16.0 was used for analyses, georeferencing, comparison, map preparation, and layout.

3.3. Implication of remote sensing

As Libya is a country located in semi-arid regions of northern Africa, the accessibility of geological features isn't convenient by a conventional field survey method. As the study area is in a desert area, the outcrops are affected by long weathering periods due to the climate. The morphology of the area is dominantly planar, and diverse lithology is associated with the outcropping hills and mesas. Due to the lack of vegetation, the lithology can be identified by using Sentinel -2 bands. As a result, extracting Earth materials information from various analyses applied to remote sensing datasets is ideal for investigating the potential of multispectral datasets in identifying mineralized zones and geological mapping in the Al Kufrah Basin. The geological map of the Al Kufrah Basin is used as ground control for analyzing remote sensing datasets.

3.4. Mapping

Individual bands of Sentinel-2 images can't display features of interest as the images are displayed in grey scales. Although the human eye can distinguish about 30 grey levels in the black-white range (Drury, 2001), It is more sensitive to color variations and patterns (Rafatirad, n.d.). Sentinel 2 data was chosen to highlight altered minerals. Several studies have been done on Sentinel-2 images combined with hyperspectral images by spectrally lowering the resolution to explore iron mineral characteristics, demonstrating the Sentinel-2 data's potential to catch iron-induced features (Mielke et al., 2014; van der Werff & van der Meer, 2015).

3.4.1. Band Ratio (BR)

The band ratio technique has been applied for the Sentinel-2 images. Several band ratios have been conducted on spectral bands VNIR bands (B2, B3, B4, and B8) and SWIR bands (B11 and B12) at 10 m resolution. Many band ratios used in previous studies were used to detect some zones with anomalies in iron deposits. The eight band ratios that have been tested to highlight the needed result is listed in table 6. The band highlights a different group of alteration minerals, including Ferric iron, Fe^{3+}, Ferrous iron, Fe^{2+}, Laterite, Gossan, Ferrous silicates, and Ferric oxides.

Table 6. Band ratio of Sentinel-2 bands applied for iron deposits

Feature	Sentinel 2A
All iron Oxide	4/2
Ferrous iron oxides	4/11
Ferric iron, Fe3+	4/3
Ferrous iron, Fe2+	12/8+3/4
Hydroxyl bearing alteration	11/12
Gossan	11/4
Ferrous silicates	12/11
Ferric oxides	11/8

3.4.2. False Color Composite (FCC)

As the false-color image depicts color composites that show wavelengths that the human eye cannot see, selecting three bands composite image wasn't as easy. FCC analysis was carried out for visualization discriminating geologic features of the study area. The FCC plays an important role when applying to the VNIR/SWIR bands of Sentinel 2. Abulghasem et al. (2011) used RGB image combinations of 7-4-2 of the ETM+ band for studying geological discriminations. A correspondence RGB color composite was applied from the individual band sets of bands 12,8,3 composite for surface lithological analysis.

The impact of various band ratios and their combinations were tested. Abram's ratio, Chica-Olma ratio, Kaufman 's ratio, and Sultan's ratio were all examined as recommended combinations to highlight geological characteristics (after Mwaniki et al., 2015). Three of the most common Ratio composite images were utilized to map ferruginous deposits as well as distinguish between different rocks. The RGB ratio composite of Sentinel-2 images used to enhance the ferruginous sediments was 4/2-11/8-11/12 blue (Sabins, 1999; CSIRO., 2003).

3.4.3. Principal Component Analysis (PCA)

Principal component analysis band selection analysis depends on the three greatest eigenvalues and their correspondence eigenvector (Bengal, 2013). Only nine bands(2, 3, 4, 5, 6, 7, 8, 8a,11, 12) of the 13 Sentinel-2 bands are suitable for geological purposes on PCA, and band 8 has a wide bandwidth; hence it is excluded, while bands with 60m resolution are also excluded (Salehi et al., 2019). Because the original image bands are so closely related, establishing PCA bands has the effect of providing new independent transformed bands and possibly reducing the number of bands required (Chapman, 2020). The PCA transformation was employed using ENVI on the 9 Sentinel bands. Because PCA was performed using the correlation matrix, the eigenvector entries also serve as loadings (correlations between the input band and the output component) without any additional computations. Based on the assessment of eigenvector loadings in each 9PCs, the PC images containing information linked to the spectral signatures of specific features of interest were chosen (Table 8). The first three principal components can be represented in an RGB composite.

3.5. Image Classification

In this thesis project, unsupervised classification has been applied using ENVI software. This method is beneficial when there is a scarcity or high cost of quality training data, as well as when there is minimal information about the data. The two widely used algorithms of unsupervised classification applied in this study were K-means and Iso-data. Clusters in multidimensional attribute space are determined using spectral reflectance from various bands. For categorization, multispectral and hyperspectral images are often utilized (Ducart et al., 2016).

The classification was performed in the PCA results of the first three PCs (PC1-PC2-PC3) with the highest eigenvalues of 99.6245510 %, 0.265299 %, and 0.060897 %, respectively. The K-mean and Iso-data was set up with 10 number of maximum iterations, 5% of change threshold, and 16 classes. The number of classes has been chosen based on the number of lithologies that covers the area, which is 16.

CHAPTER FOUR: DISCUSSION AND RESULT

The result of image analysis on the Sentinel-2 datasets and along with a discussion, are presented in this chapter. The results of image analyses of Sentinel-2 data are used to demonstrate the findings on the ferruginous deposit, mapping, and image classification are presented in the same order as the Methodology chapter. Finally, the results were cross-checked against the generalized geological map for validation.

4.1. Image Analysis

The general lithologies overall lithologies in the study area are listed in the legend with the Index in table 7. Two separate geological maps were prepared, one based on the number of lithologies and the other one on geological time formations of the lithologies (figure 3A and figure 3B), respectively. On the map, the Cenozoic ferruginous sediments are labeled with the legend name of CzI.

4.2. Band Ratio Images

Different band ratio and their combination were tested. Of the most commonly used combinations, three were applied to map the ferruginous sediments and discriminate the rocks. Abram's ratio combination was good at discriminating lithologic structures, whereas Kaufmann's ratio didn't differentiate between various lithologic units. Chica-Olma ratio composite using 4/2-11/8-11/12 gave a good result.

The band ratio of 4/2 is sensitive to iron even in low concentrations; hence the iron oxide is widespread in the northeastern part of the area in red color. Sandstone, siltstone, and claystone are the underlying rocks in this region. The presence of ferrous and clay minerals is denoted by the presence of green color, including sandstone, siltstone, claystone, conglomerate, and kaolinitic siltstone. The shades of blue that can be seen on the site are within the lateritic, which indicates the presence of ferrous as well as clay and very few iron oxides (figure 4A). Regarding the geology of the study area, which covers various lithology, the contact between each rock was not clearly mapped by the applied method. The band ratios played a significant role only in highlighting the iron oxide, ferruginous sediments, laterite, and geologic units. When compared to the findings obtained using the same methodology by Mia, B., & Fujimitsu (2012), the results obtained using the Chica-Olma ratio that was employed in the research area showed a high degree of concordance.

4.3. False Color Composite

The employment of band triplets of Sentinel- 2 bands of 12-8-3 in the creation of FCC improved various lithologic units. The Holocene sand deposits area appears a pale violet color, and the lateritic deposits are displaying as a pale yellow (figure 1). The Cretaceous and Permian sedimentary succession appear in a dull green colors and black color.

A comparison was made between the previously published RGB images (El-Liel et al., 2017). The present study's findings confirm the notion that the color composite image is useful for the newly developed Sentinel datasets.

4.4. Principal Component Analysis

This analysis produces PC bands and statistics containing the eigenvectors, covariance matrix, and eigenvalues. The eigenvectors matrix is used to identify the PC bands that contain the spectral information of specific minerals. The eigenvector matrix for the principal component analysis (PCA) transformation of Sentinel bands, which resulted in 9 PC outputs, is summarized in Table 7. Following the application of the principal component transformation, it has been determined that the first principal component, denoted by PC1, is composed of a positive weighing of total bands. The PC1 accounts for the maximum variance, which is approximately 99.62%. The utilized RGB composite of PC1-PC2-PC3 is shown in figure 4B, which gives results in discerning geologic lithologies. Even though the geologic contrast is readily apparent in the combination, some lithologic units share similar colors. For instance, the laterite and neighboring lithologies both appear in pale orange color. The weakness of the PCA method is the difficulty in interpreting a color composite from PC (Chavez, P.S., Jr, Kwarteng, 1989). When PC1 is excluded, the image can lack contrast. But PCA analyzed images can be useful for classification analysis.

4.5 Image Classification

The classification resulted in classifying the lithologies based on the spectral signature of the rocks. The result for lithologic mapping of the two algorithms were compared; the rock units were well-classified using K-mean and Iso-data classifier for the study area.

Figure 5A and 5B show the K-mean and Iso-data classified map using three PC inputs of PC1, PC2, and PC3. Both classifications resulted in 16 classes (1, 2, 3, 4, 5, 6, 7 ,8, 9, 10, 11, 12, 13, 14, 15, and 16). The K- mean classification map of the study area was considered the best result for lithologic discrimination in the geologic lithology. The result of the classification map of the area using the Iso-data algorithm was considered the best candidate for the geologic map of the area.

Zonal statistics operation was analyzed to produce statistics on cell values of a raster (a value raster) that is contained inside the zones defined by a different dataset (geological map). As a result, both algorithms assigned the ferruginous sediment deposit in the same class. No lithology has been assigned to classes number, 1,2, and 3 which covers only 0.13% of the total study area. The Cenozoic ferruginous deposits are concentrated in the assigned classes of (11,12,14,15), distributed from less to a high concentration of possible iron. 57 % of the pixel count of the ferruginous sediment is assigned to class 14 (Table 9).

This classification of PCA of Sentinel 2 data appears to reasonably represent the surface geology character of the distribution of ferruginous sediments in the area. Nevertheless, the K-mean classified image was consistent with the geological map that was used as a reference for the area. The percentage of the area of a polygon for each lithology in the geological map and the total count of a pixel of lithology in the classified image rank the lithologies in the same rank. Cenozoic ferruginous sediments were approximately covering 4 % of the area on the geological map, whereas in the classified image (K- mean classification), the sediment has 2 % occurrence on the classified image.

Table 7. Geological Index of the lithology

Geologic Indices			
Geologic Time	**Symbol**	**Formation**	**Composition**
HOLOCENE	Qed	Eolian sediments, sand dunes	Sand
	Qes	Eolian sediments, sand sheets	Sand, fine gravel
	Qf	Fluvial sediments	Unconsolidated clay, silt, sand, and gravel
	Qw	Wadi deposits	Gravel, sand, silt, and loam
PLEISTOCENE - HOLOCENE	Qpl	Playa deposits	Siltstone, clayey siltstone, gravel, calcrete
	Qd	Colluvial and slope deposits	Slope debris, sand, sandy silt
	Qg	Serir	Gravel, sand, rock debris of fluvial, pluvial origin with eolian reworking
	Qp	Proluvial sediments, alluvial fan	Rock debris, sand, and silt, locally cemented
PLEISTOCENE	Qo	Old wadi sediments	Unconsolidated gravel, sand, and silt
	Qop	Old proluvial sediments, old alluvial fan	Unconsolidated gravel, sand, and silt
	Qlc	Lacustrine deposits	Rock debris, sand, and silt, locally cemented
	Qs	Sabkha sediments	Salt, gypsum, gypsiferous clay
	Qn	Nabkha sediments	Salty sand, gypsum
OLIGOCENE	B	Basalt, fonolite	Basalt, olivine basalt, microporphyric basalt, phonolite
CENOZOIC	Czl	Idrisi Formation	In situ weathering product, laterite, duricrust, ferruginous, locally redeposited
	Czc	Continental sediments in general	Gravel, rock debris, sand, silt, locally cemented, often ferruginous
CRETACEOUS	KN	Al Jawf Formation* / Nubia Formation	Sandstone, siltstone, claystone and conglomerate
PERMIAN-LOWER CRETACEOUS	PKIQ	Quarat Al Hamra Formation	Sandstone, siltstone, claystone, and conglomerate, kaolinitic siltstone
	PKIQR	Rabyanah Member (Quarat Al HamraFm.)	Lacustrine marl and limestone
CARBONIFEROUS	CZ	Az Zalmah Formation	Intercalations of siltstone, claystone, shale, sandstone, Kaolinitic sandstone, and conglomerate

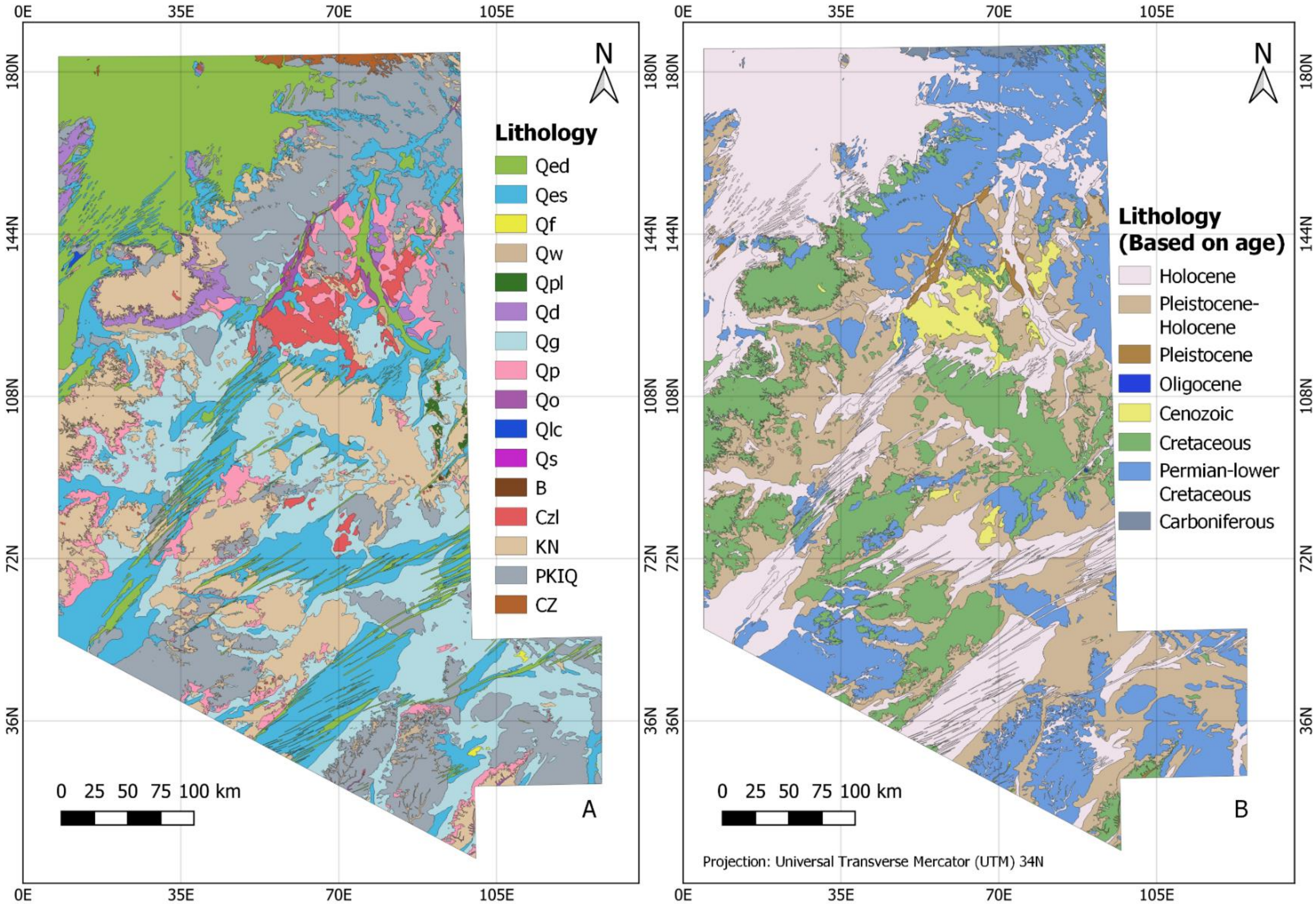

Figure 3. Geologic map: (a) geological lithology, (b) geologic time of formations

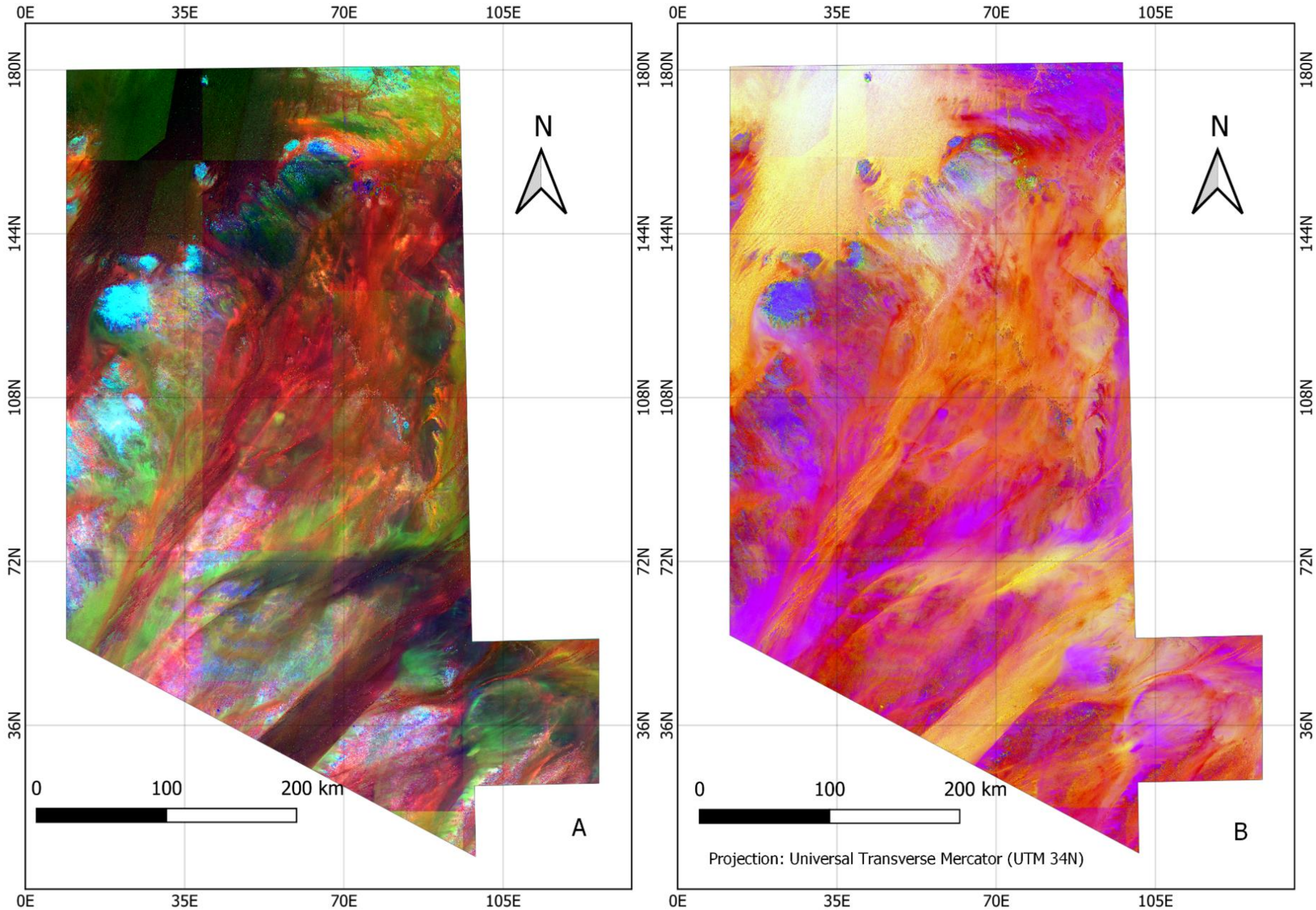

Figure 4. A: RGB band ratio of Sentinel-2 band (4/2-11/8-11/12) and B: PCA (pc1-pc2-pc3)

Table 8. PCA of Sentinel-2 Bands

Input Bands	Band 2	Band 3	Band 4	Band 5	Band 6	Band 7	Band 8a	Band 11	Band 12	
Band Means	1021.643215	1893.400586	3142.935464	3460.140970	3579.554360	3646.566601	3611.092908	4748.168279	4304.686683	
Band StdDev	745.865581	1342.494856	2173.216580	2383.691890	2461.528759	2508.718809	2494.389818	3230.632576	2953.331833	
Eigen Vector Matrix										**Eigen Value (%)**
PC1	0.101353	0.186761	0.305978	0.335925	0.346949	0.353620	0.351417	0.454386	0.415930	**99.624551**
PC2	0.484604	0.559192	0.219742	0.107344	0.021312	0.033379	0.189492	-0.554782	-0.217704	**0.265299**
PC3	0.461880	0.386662	-0.249680	-0.275243	-0.298643	-0.254877	-0.243479	0.386027	0.369610	**0.060897**
PC4	0.152230	0.099129	0.187170	0.086871	0.086051	0.005594	-0.241109	0.540526	-0.752783	0.028410
PC5	0.257038	-0.105034	-0.790257	0.065505	0.143786	0.227898	0.411835	0.064003	-0.218601	0.011989
PC6	0.529910	-0.615875	0.345086	-0.182736	-0.187869	-0.166730	0.349089	0.048832	-0.008689	0.003818
PC7	0.354757	-0.293295	-0.118329	0.616538	0.231789	-0.124355	-0.525475	-0.153561	0.158459	0.003128
PC8	-0.208916	0.111197	-0.050019	0.575442	-0.434965	-0.521611	0.362615	0.119481	-0.057584	0.001671
PC9	-0.044802	0.066110	-0.024995	-0.208303	0.695478	-0.664505	0.155237	0.015071	0.005056	0.000236

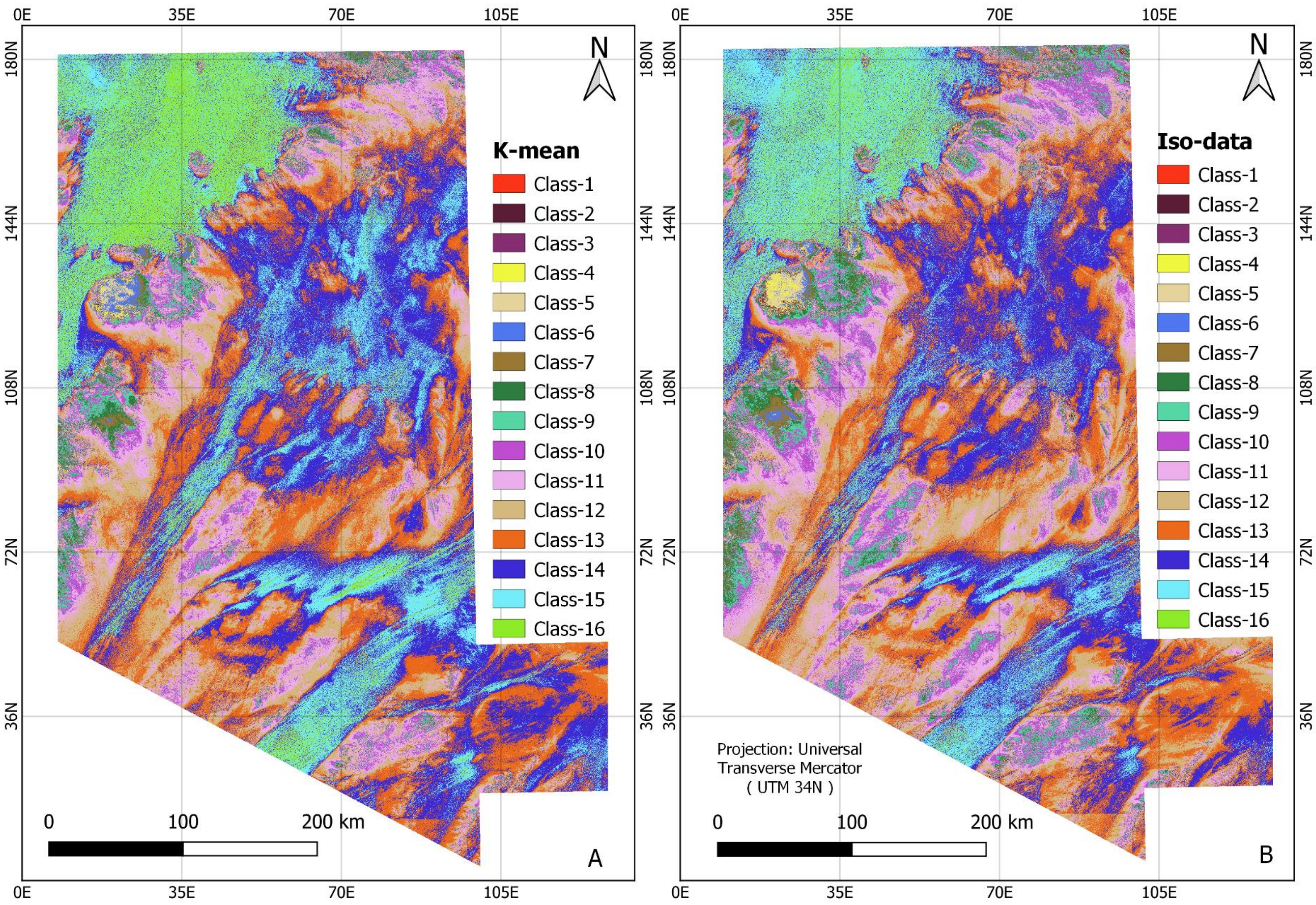

Figure 5. K-Mean and Iso-data Classification On (PC1-PC2-PC3): A And B, respectively

Table 9. Zonal statistics on Classified image

Geological-Lithology	Assigned Classes in Percentage (%) of the pixel count in each class																		
	C-1	**C-2**	**C-3**	**C-4**	**C-5**	**C-6**	**C-7**	**C-8**	**C-9**	**C-10**	**C-11**	**C-12**	**C-13**	**C-14**	**C-15**	**C-16**	**Total %**	**Pixel wise distribution**	**Polygon wise distribution**
Qed	0	0	0	0	0	0	0	0	0	0	1	1	5	23	9	61	100%	12	9
Qes	0	0	0	0	0	0	0	0	0	0	2	8	17	35	30	8	100%	17	17
Qf	0	0	0	0	0	0	0	0	0	0	0	7	54	38	1	0	100%	0.06	0.1
Qw	0	0	0	0	0	0	1	1	3	11	26	25	18	13	2	0	100%	1	2
Qpl	0	0	0	0	0	0	0	1	2	4	11	35	37	9	1	0	100%	0.1	0.3
Qd	0	0	0	2	1	1	1	2	9	18	21	16	11	12	4	2	100%	2	4
Qg	0	0	0	0	0	0	0	0	0	1	6	16	33	34	10	0	100%	21	12
Qp	0	0	0	0	0	0	0	1	3	9	13	17	13	32	12	0	100%	5	11
Qo	0	0	0	0	0	0	0	0	0	0	1	5	14	30	48	2	100%	0.3	1
Qlc	0	0	0	0	0	0	0	0	1	2	5	9	15	35	26	7	100%	0.1	0.2
Qs	0	0	0	0	0	0	0	0	0	0	0	0	1	52	44	3	100%	0.03	0.08
Betab	0	0	0	0	0	0	1	3	7	12	21	25	21	9	1	0	100%	0.01	0.02
Czl	0	0	0	0	0	0	0	0	0	1	1	8	14	57	18	1	100%	2	4.3
KN	0	0	0	1	2	2	3	4	6	9	15	20	21	14	3	0	100%	16	18
PKIQ	0	0	0	0	0	0	0	1	2	5	13	19	29	27	4	0	100%	23	20
CZ	0	0	0	0	1	3	7	9	10	12	10	8	8	13	16	3	100%	0.4	1
% TC	**0.01**	**0.04**	**0.08**	**0.2**	**0.4**	**0.55**	**0.72**	**1**	**2**	**4**	**8**	**14**	22	27	11	9	100%	**100%**	**100%**

***C: Class *TC: Pixel count of each class in the area**

Pixel wise distribution = (Pixel count of individual lithology/total pixel count of all lithology in the area) *100

Polygon wise distribution = (Area of polygons of an individual lithology/total Area of polygons of all lithology) *100

CHAPTER FIVE: CONCLUSION AND RECOMMENDATIONS

The results of this study demonstrate that remote sensing techniques are effective techniques for geological mapping and mineral exploration. The result shows around 57 % of the Cenozoic ferruginous sediments are assigned to class 14 in the classification. Different processing approaches were used to identify and delineate lithological units using Sentinel-2 images to identify and map the ferruginous concentrated iron sediments in the Al Kufrah Basin. This study demonstrates that the standard color composite and color composite images created using PCA are useful for distinguishing between lithologies.

False-color composite images enhance the appearance of distinct lithologic units and structures more than a single band image would. Ratio images and their combination, such as the Chica-Olma ratio faceplate, the recognition of iron oxides, and hydrothermal alteration. In this study, the iron-concentrated ferruginous deposits were clearly recognized using the Chica-Olma ratio.

PCA approach applied to the Sentinel -2 bands reduces the correlation between spectral bands. PCA analysis produced inconsistent outcomes in terms of improving geologic feature discrimination. Bands with the greatest variance are separated and saved in the three PC bands. The creation of color composite images by combining the three PCs improves and facilitates the visual discrimination of geologic units and features that are not improved in ordinary color composite images.

Utilizing the K-mean and Iso-data classification algorithms, unsupervised classification turned into a good lithology classification. The result of the identification of ferruginous sediments suggests the presence of an iron deposit, confirming the results of the earlier geological mapping. The classification revealed that ferruginous deposits are widespread throughout the area, but prospective iron-rich ferruginous sediment is concentrated in the central part of the area, specifically in the northeastern portions, while field investigations supported the same findings. The finding of widespread sediment distribution may suggest the deposit

The study also demonstrated the significance of remote sensing analysis for geologic data collection prior to fieldwork. Remote sensing techniques give detailed information, which allows for the mapping of mineral deposits even though the concentration of minerals cannot be directly measured. The fact that remote sensing data can be downloaded for free significantly increases the value of remote sensing analysis for mineral exploration and geologic mapping.

Though the use of Sentinel-2 data enabled the discrimination of different geologic features and the mapping of the distribution of ferruginous concentrations in the Al Kufrah Basin, it is expected that further study using a variety of methodologies could yield even better findings for the extension of the iron deposits. The mineral can be found in sedimentary iron deposits, from which practically almost all iron is deposited.

PCA approaches can be implemented in oriented (Crósta technique/Feature-oriented (FPCS)/developed selective PC) techniques (El Zalaky M.A et al., 2018) for better results in finding iron oxide and Hydrothermal alterations. To determine the applicability of the remote sensing techniques and analysis approaches used in this work in other locations, they should be evaluated in mineral and geologic mapping applications in other regions. Due to time, the investigation was focused mainly on the Cenozoic ferruginous sediments of the Al Kufrah Basin. If appropriate funding and time are made available, the study can be expanded to explore and validate the other lithologies in the area with appropriate approaches.

REFERENCE

A. Ali, E. (2012). Landsat ETM+7 Digital Image Processing Techniques for Lithological and Structural Lineament Enhancement: Case Study Around Abidiya Area, Sudan. The Open Remote Sensing Journal, 5(1), 83–89. https://doi.org/10.2174/1875413901205010083

Abdunaser, K. M. (2015). Satellite Imagery for Structural Geological Interpretation in Western Sirt Basin, Libya: Implication for Petroleum Exploration. Geosciences, 5(1), 8–25. https://doi.org/10.5923/j.geo.20150501.02

Abrams, J.M., Brown, D., Lepley, L., Sadowski, R. (1983). Remote sensing for porphyry copper deposits in Southern Arizona. Economic Geology, 78, 591–604.

Abrams, M. J., Rothery, D. A., & Pontual, A. (1988). Mapping in the Oman ophiolite using enhanced Landsat Thematic Mapper images. Tectonophysics, 151(1–4), 387–401. https://doi.org/10.1016/0040-1951(88)90254-5

Abulghasem, Y. A., Akhir, J. B. M., Hassan, W. F. W., Samsudin, A. R., & Youshah, B. M. (2012). The use of remote sensing technology in geological investigation and mineral detection in Wadi shati, Libya. Electronic Journal of Geotechnical Engineering, 17 I(January 2012), 1279–1291.

Abulghasem, Y. A., Akhir, J. M., Samsudin, A. R., Hassan, W. F. W., & Youshah, B. M. (2011). Integrated data of remote sensing and geophysical data for iron ore exploration in the western part of Wadi Shatti district, Libya. Electronic Journal of Geotechnical Engineering, 16 P(March), 1441–1454.

Agar, B., & Coulter, D. (2007). Remote Sensing for Mineral Exploration – A Decade Perspective 1997-2007. Exploration in the New Millennium, Proceedings of the Fifth Decennial International Conference on Mineral Exploration, m, 109–136.

Alasta, A. F. (2011). Using Remote Sensing data to identify iron deposits in central-western Libya Resolution Enhancement using Wavelet Transforms applied to SODSIM Images View project. December 2011. https://www.researchgate.net/publication/325550303

Albert G., Trish KB. (eds.), Császár G., Csillag G., Csontos P., El-Grewi AM., El-Mehdi BO., Fodor L., Kalmár J., Loránt. M. Mabrouk JB. (2016). Explanatory Booklet for the Geological map of Libya, 1: 250,000, Sheet: East Iraq al Idrisi NF 35-13. Industrial Research Center, Tripoli, 133 p, 1–108.

Albert, G., & Ammar, S. (2020). Application of machine learning and remotely sensed data in geological mapping on the Jebel Meloussi area (Tunisia) Application of machine learning and remotely sensed data in geological mapping on the Jebel Meloussi area (Tunisia). November, 0–4.

Aydda, A., Althuwaynee, O. F., & Pokharel, B. (2020). An easy method for barchan dunes automatic extraction from Multispectral Satellite Data. IOP Conference Series: Earth and Environmental Science, 419(1), 012015. https://doi.org/10.1088/1755-1315/419/1/012015

Bengal, W. (2013). Optimum Index Factor (OIF) for Landsat Data: a Case Study on Barasat Town, International Journal of Remote Sensing & Geoscience (IJRSG), 2(5), 11–17.

Chapman, J. S. (2020). A Primer for the use of Satellite Imagery in Geologic Investigations. May, 45. https://doi.org/10.13140/RG.2.2.26594.15040

Ciampalini, A., Garfagnoli, F., Del Ventisette, C., & Moretti, S. (2013). Potential Use of Remote Sensing Techniques for Exploration of Iron Deposits in Western Sahara and Southwest of Algeria. Natural Resources Research, 22(3), 179–190. https://doi.org/10.1007/s11053-013-9209-5

Colwell, R. (1983). Manual of remote sensing. American Society of Photogrammetry and Remote Sensing, Falls Church., 1 and 2.

CSIRO. (2003). . http://www.syd.dem.csiro.au/research/MMTG/Exploration/ASTER/ASTER.htm.

Drury, S. A. (2001). Image interpretation in geology. Nelson Thornes Blackwell Science, Cheltenham Malden.

El Atillah, A., El Atillah, M., El Morjani, Z. E., Elfazazy, K., & Souhassou, M. (2021). Segmentation and classification algorithms applied to Sentinel-2a images for geological mapping: Case of the Al Glo'a Sheet (1/50000), Morocco. Bulletin Of The Mineral Research and Exploration, 1–20. https://doi.org/10.19111/bulletinofmre.864492

El Atillah, A., El Morjani, Z. E. A., & Souhassou, M. (2019). Use of the Sentinel-2A Multispectral Image for Litho-Structural and Alteration Mapping in Al Glo’a Map Sheet (1/50,000) (Bou Azzer-El Graara Inlier, Central Anti-Atlas, Morocco). Artificial Satellites, 54(3), 73–96. https://doi.org/10.2478/arsa-2019-0007

El Atillah, A., El Morjani, Z. E., & Souhassou, M. (2019). Use of the Sentinel-2a multispectral image for litho-structural and alteration mapping in Al Glo’a Map Sheet (1/50,000) (Bou Azzer–el graara inlier, central anti-atlas, Morocco). Artificial Satellites, 54(3), 73–96. https://doi.org/10.2478/arsa-2019-0007

El Zalaky M.A, Essam M. Esmail, & El Arafy R.A. (2018). Assessment of Band Ratios and Feature-oriented principal component selection (FPCS) Techniques for Iron Oxides Mapping with relation to radioactivity using Landsat 8 at Bahariya Oasis, Egypt. Researcher, 10(4), 1–10. https://doi.org/10.7537/marsrsj100418.01

European Space Agency. (2022). Resolution and Swath. Sentinel. Retrieved 21st March 2022, from https://sentinels.copernicus.eu/web/sentinel/missions/sentinel-2/instrument-payload/resolution-and-swath

Gazley, M. F., Collins, K. S. S., Hines, B. R. R., Fisher, L. A. A., & McFarlane, A. (2015). Application of principal component analysis and cluster analysis to mineral exploration and mine geology and cluster analysis to mineral exploration. AusIMM New Zealand Branch Annual Conference 2015, September 131–139.

Ge, W., Cheng, Q., Tang, Y., Jing, L., & Gao, C. (2018). Lithological classification using Sentinel-2A data in the Shibanjing ophiolite complex in Inner Mongolia, China. Remote Sensing, 10(4). https://doi.org/10.3390/rs10040638

Ghoneim, E. (2018). Rimaal: A sand buried structure of possible impact origin in the Sahara: Optical and radar remote sensing investigation. Remote Sensing, 10(6). https://doi.org/10.3390/rs10060880

Ghoneim, E. M. (2009). Ibn-Batutah: A possible simple impact structure in southeastern Libya, a remote sensing study. Geomorphology, 103(3), 341–350. https://doi.org/10.1016/j.geomorph.2008.07.005

Ghoneim, E., Benedetti, M., & El-Baz, F. (2012). An integrated remote sensing and GIS analysis of the Kufrah Paleoriver, Eastern Sahara. Geomorphology, 139–140, 242–257. https://doi.org/10.1016/j.geomorph.2011.10.025

GISGeography. (2021). Sentinel 2 Bands and Combinations. GIS Geography, Retrieved 24th March 2022, from https://gisgeography.com/sentinel-2-bands-combinations/

GISGeography. (2021, October 29). Image classification techniques in remote sensing. GIS Geography. Retrieved 29th March 2022, from https://gisgeography.com/image-classification-techniques-remote-sensing/.

Goudarzi GH. (1970). Geology and Mineral Resources of Libya. a Reconnaissance. US Geological Survey Professional Paper.

Ibrahim, E., Barnabé, P., Ramanaidou, E., & Pirard, E. (2018). Mapping mineral chemistry of a lateritic outcrop in new Caledonia through generalized regression using Sentinel-2 and field reflectance spectra. International Journal of Applied Earth Observation and Geoinformation, 73, 653–665. https://doi.org/10.1016/J.JAG.2018.08.004

Kalinowski, A., & Oliver, S. (2004). ASTER processing manual. Geoscience Australia, 37(October), 1–40.

Khaleghi, M., Ranjbar, H., Abedini, A., & Calagari, A. A. (2020). Synergetic use of the Sentinel-2, ASTER, and Landsat-8 data for hydrothermal alteration and iron oxide minerals mapping in a mine scale. Acta Geodynamica et Geomaterialia, 17(3), 311–328. https://doi.org/10.13168/AGG.2020.0023

Koeberl, C., Reimold, W. U., & Plescia, J. (2005). BP and Oasis Impact Structures, Libya: Remote Sensing and Field Studies. Impact Tectonics, 161–190. https://doi.org/10.1007/3-540-27548-7_6

Lillesand, T., R. Kiefer., J. C. (2004). Remote sensing and Image Interpretation. Fifth Edit(John Wiley and Sons).

Lin, J., Wang, R., Zhao, B., & Cheng, S. (2019). A comprehensive scheme for lithological mapping using Sentinel-2A and ASTER GDEM in the weathered and vegetated coastal zone, Southern China. Open Geosciences, 11(1), 982–996. https://doi.org/10.1515/geo-2019-0076

Liu, F., Wu, X., Sun, H., Guo, Y. (2007). Alteration information extraction by applying synthesis processing techniques to Landsat ETM+ data: case study of Zhaoyuan Gold Mines Shandong Province, China. Journal of China University of Geosciences, 18, 72–76.

Loughlin, W. P. (1991). Principal component analysis for alteration mapping. Photogrammetric

Engineering & Remote Sensing, 57(9), 1163–1169.

Marrakchi, O. (2013). Elaboration of texture signatures of remote sensing images. Remote Sensing, 11 (2), 337–350. https://halshs.archives-ouvertes.fr/halshs-01136470/

Marrakchi, O. C., Charfi, C. M., Hamzaoui, M., & Habaieb, H. (2021). Improvement of Sentinel-1 Remote Sensing Data Classification by DWT and PCA. https://doi.org/10.1155/2021/8897303

Masoumi, F., Eslamkish, T., Honarmand, M., & Abkar, A. A. (2016). A Comparative Study of Landsat-7 and Landsat-8 Data Using Image Processing Methods for Hydrothermal Alteration Mapping. Resource Geology, 67(1), 72–88. https://doi.org/10.1111/rge.12117

Memarsadeghi, N., Mount, D. M., Netanyahu, N. S., & Le Moigne, J. (2003). A Fast Implementation of the ISOCLUS Algorithm. International Geoscience and Remote Sensing Symposium (IGARSS), 3, 2057–2059. https://doi.org/10.1109/igarss.2003.1294338

Memarsadeghi, N., Mount, D. M., Netanyahu, N. S., & Le Moigne, J. (2007). A fast implementation of the iso data clustering algorithm. International Journal of Computational Geometry and Applications, 17(1), 71–103. https://doi.org/10.1142/S0218195907002252

Mielke, C., Boesche, N. K., Rogass, C., Kaufmann, H., Gauert, C., & de Wit, M. (2014). Spaceborne mine waste mineralogy monitoring in South Africa, applications for modern push-broom missions: Hyperion/OLI and EnMAP/Sentinel-2. Remote Sensing, 6(8), 6790–6816. https://doi.org/10.3390/rs6086790

Mohamed, M. T. A. M., Al-Naimi, L. S., Mgbeojedo, T. I., & Agoha, C. C. (2021). Geological mapping and mineral prospectivity using remote sensing and GIS in parts of Hamissana, Northeast Sudan. Journal of Petroleum Exploration and Production, 11(3), 1123–1138. https://doi.org/10.1007/s13202-021-01115-3

Nivedita Priyadarshini, K., Kumar, M., Rahaman, S. A., & Nitheshnirmal, S. (2018). A comparative study of advanced land use/land cover classification algorithms using Sentinel-2 data. The International Archives of the Photogrammetry, Remote Sensing and Spatial Information Sciences, XLII-5, 665–670. https://doi.org/10.5194/isprs-archives-xlii-5-665-2018

Nurdin, N., Supriadi, S., Lanuru, M., Akbar As, M., Kartika, I., & Komatsu, T. (2019). Accuracy of unsupervised classification to determine coral health using spot-6 and Sentinel-2a. International Archives of the Photogrammetry, Remote Sensing and Spatial Information Sciences - ISPRS Archives, 42(4/W16), 503–509. https://doi.org/10.5194/isprs-archives-XLII-4-W16-503-2019

Oppenheimer, C. (2000). RICHARDS, J. A. & J IA X IUPING . 1999. Remote Sensing Digital Image Analysis. An Introduction, 3rd revised and enlarged edition. xxi + 363 pp. Berlin, Heidelberg, New York, London, Paris, Tokyo, Hong Kong: Springer-Verlag. Price DM 139.00, Ös 1015.00, SFr 126.50, £53.30, US $89.95 (hard covers). ISBN 3 540 64860 7. Geological Magazine, 137(3), 335–342. https://doi.org/10.1017/S0016756800294132

Rafatirad, S. (n.d.). Sensitivity to color variations & Spatial Localization. 1–26.

http://www.ics.uci.edu/~majumder/vispercep/paper08/spatialvision.pdf

Rajendran, S., Thirunavukkarasu, A., Balamurugan, G., & Shankar, K. (2011). Discrimination of iron ore deposits of granulite terrain of Southern Peninsular India using ASTER data. Journal of Asian Earth Sciences, 41(1), 99–106. https://doi.org/10.1016/j.jseaes.2011.01.004

Richards, J. A. (2013). Multisource Image Analysis. In: Remote Sensing Digital Image Analysis. Springer, Berlin, Heidelberg. https://doi.org/10.1007/978-3-642-30062

Richards, J.A. & Xiuping, J. (1999). Remote sensing digital image analysis. Berlin Heidelberg, Springer. https://doi.org/10.1007/978-3-662-%0A03978-6

Sabins, F. F. (1999). Remote sensing principles and interpretation. Ore Geology Review, 14(Elsevier), 157–183.

Salehi, S., Mielke, C., Brogaard Pedersen, C., & Dalsenni Olsen, S. (2019). Comparison of ASTER and Sentinel-2 spaceborne datasets for geological mapping: A case study from North-East Greenland. Geological Survey of Denmark and Greenland Bulletin, 43, 1–6. https://doi.org/10.34194/GEUSB-201943-02-05

Schmieder, M., Buchner, E., & Le Heron, D. P. (2009). The Jebel Hadid structure (Al Kufrah Basin, SE Libya)-A possible impact structure and potential hydrocarbon trap? Marine and Petroleum Geology, 26(3), 310–318. https://doi.org/10.1016/j.marpetgeo.2008.04.003

Sekandari, M., Masoumi, I., Pour, A. B., Muslim, A. M., Rahmani, O., Hashim, M., Zoheir, B., Pradhan, B., Misra, A., & Aminpour, S. M. (2020). Application of Landsat-8, Sentinel-2, ASTER, and Worldview-3 spectral imagery for exploration of carbonate-hosted Pb-Zn deposits in the Central Iranian Terrane (CIT). Remote Sensing, 12(8). https://doi.org/10.3390/RS12081239

Soydan, H., Koz, A., & Düzgün, H. Ş. (2021). Secondary Iron Mineral Detection via Hyperspectral Unmixing Analysis with Sentinel-2 Imagery. International Journal of Applied Earth Observation and Geoinformation, 101. https://doi.org/10.1016/j.jag.2021.102343

Tangestani, M. H., & Shayeganpour, S. (2020). Mapping a lithologically complex terrain using Sentinel-2a data: A case study of Suriya area, southwestern Iran. International Journal of Remote Sensing, 41(9), 3558–3574. https://doi.org/10.1080/01431161.2019.1706203

Tangestani, M. H., Mazhari, N., Agar, B., and Moore, F. (2008). Evaluating advanced spaceborne thermal emission and reflection radiometer (ASTER) data for alteration zone enhancement in a semi-arid area, northern Shahr-e-Babak, Se Iran. International Journal of Remote Sensing, 29(10), 2833–2850. https://doi.org/10.1080/01431160701422239

The University of Oviedo. (n.d.). K-means algorithm applied to image classification and processing. K-means. Retrieved 29th March 2022, from https://www.unioviedo.es/compnum/labs/new/kmeans.html

Van der Meer, F. D., van der Werff, H. M. A., & van Ruitenbeek, F. J. A. (2014). Potential of ESA's Sentinel-2 for geological applications. Remote Sensing of Environment, 148(June), 124–133. https://doi.org/10.1016/j.rse.2014.03.022

van der Werff, H., & van der Meer, F. (2015). Sentinel-2 for mapping iron absorption feature parameters. Remote Sensing, 7(10), 12635–12653. https://doi.org/10.3390/rs71012635

van der Werff, H., & van der Meer, F. (2016). Sentinel-2A MSI and Landsat 8 OLI provide data continuity for geological remote sensing. Remote Sensing, 8(11). https://doi.org/10.3390/rs8110883

van der Werff, H., van der Meer, F., Jin-King Liu, J., Soares Galvao, L., Baghdadi, N., & Thenkabail, P. S. (2015). Remote Sens. 7, 12635–12653. https://doi.org/10.3390/rs71012635

Van Gasselt, S., Kim, J. R., Choi, Y. S., & Kim, J. (2017). The Oasis impact structure, Libya: Geological characteristics from ALOS PALSAR-2 data interpretation. Earth, Planets and Space, 69(1). https://doi.org/10.1186/s40623-017-0620-8

Vincent, R. . (1997). Fundamentals of geological and environmental remote sensing. Prentice-Hall, 366(Upper Saddle River).

Wang, R. (2016). Unsupervised Classification-Clustering. [Online](Available at:). http://fourier.eng.hmc.edu/e161/lectures/classification/node12.%0Ahtml [Accessed 6 Juni 2016].

Y. E. Abdelhady. (1978). Geophysical Analyses of Gravity data in the Northern Borderlands Between Egypt and Libya Y. Second Symposium on the Geology of Libya University of Al-Fateh Faculty of Science Geology Department.